Chapter 3

Compositional degradation with Br content in Cesium lead halide $CsPbBr_xI_{3-x}$

Publication: ***Manish Kumar***, *Vani Pawar, Priyanka A. Jha, Pardeep K. Jha, and Prabhakar Singh, Compositional degradation with Br content in Cesium lead halide $CsPbBr_xI_{3-x}$, Journal of Solid State Chemistry, 308, 122893 (2022).*

CHAPTER 3: Compositional Degradation with Br Content in Cesium Lead Halide $CsPbBr_xI_{3-x}$

3.1 Introduction

It has been discussed in chapter 1 that stability issues are the major problem in the Perovskite halide materials. However, the inorganic cesium lead halide $CsPbX_3$ (where X= I, Br, Cl) are reported to possess good stability than that of the organic-inorganic hybrid halides. $CsPbI_3$ is reported to have four phases: perovskite black phase (cubic (α), tetragonal (β), orthorhombic (γ)) and non-perovskite yellow orthorhombic (δ) [141]. With a bandgap of ~ 1.73eV, $CsPbI_3$-α is the most suitable phase among all-inorganic lead halide Perovskites. However, in the ambient atmosphere (almost instantly) the perovskite black phase converts into a non-perovskite yellow orthorhombic phase. At the same time, $CsPbBr_3$ remains in the orthorhombic phase at room temperature.

In this chapter, it is aimed to study the compositional variation of Br- at X-site of Cesium lead halide $CsPbBr_xI_{3-x}$ (x= 0.0 - 3.0 at the step of 0.5), compounds are synthesized by cold sintering technique. We have observed yellow non-perovskite phase of $CsPbI_3$ in $CsPbBr_xI_{3-x}$ (x= 0.0 – 1.0 at the step of 0.5) and compositional degradation occurred with the further increase in x. The plausible mechanism for this compositional degradation is investigated here.

3.2 Experimental details

The perovskite powders $CsPbBr_xI_{3-x}$ (x= 0.0 - 3.0 in steps of 0.5) were synthesized by the solid-state reaction route via the cold sintering method at room temperature. The particle compaction and grain growth occur at room temperature. It has been found that all the

perovskite compounds are nucleated at room temperature without calcination. The powders of CsI, CsBr, PbI_2, and $PbBr_2$ were weighed according to their mass ratio. The precursor was mixed (Humidity 60 %) and ground for 2 hours in mortar-pestle at room temperature for synthesizing $CsPbBr_xI_{3-x}$ (x= 0.0 - 3.0 in steps of 0.5). The final mixed product is converted into orange and yellow color forms. The synthesized powders were pelletized using a hydraulic press. The pellets were sintered in the vacuum oven at 80 °C for 1 h. For I-V measurements, we have used silver electrodes. The final product $CsPbBr_xI_{3-x}$ was obtained as per the following reactions.

$$CsI + PbI_2 \rightarrow CsPbI_3 \qquad (x = 0.0) \qquad 3.1$$

$$0.5\,CsBr + 0.5\,CsI + PbI_2 \rightarrow CsPbBr_{0.5}I_{2.5} \qquad (x = 0.5) \qquad 3.2$$

$$CsBr + PbI_2 \rightarrow CsPbBr_1I_2 \qquad (x = 1.0) \qquad 3.3$$

$$0.5\,CsBr + 0.5\,PbBr_2 + 0.5\,CsI + 0.5\,PbI_2 \rightarrow CsPbBr_{1.5}I_{1.5} \qquad (x = 1.5) \qquad 3.4$$

$$CsI + PbBr_2 \rightarrow CsPbBr_2I_1 \qquad (x = 2.0) \qquad 3.5$$

$$0.5\,CsI + 0.5\,CsBr + PbBr_2 \rightarrow CsPbBr_{2.5}I_{0.5} \qquad (x = 2.5) \qquad 3.6$$

$$CsBr + PbBr_2 \rightarrow CsPbBr_3 \qquad (x = 3.0) \qquad 3.7$$

The identification of the phase formation for the synthesized compounds was examined by the X-ray Diffractometer (RigakuMiniflex) with Cu-Kα radiation (λ=1.540598 Å) in the 2θ range of (5°-70°) with the step size of 0.01° at the room temperature. The surface morphology images and Energy Dispersive X-Ray analysis (EDX) of Perovskite compounds were recorded using EVO - Scanning Electron Microscope MA15/18. The optical absorption spectra of the samples were obtained by the JASCO V-770 Ultraviolet-Visible spectrometer. The thermodynamical studies of the compounds were performed using SHIMADZU DSC-60 plus

230V. The X-ray photoelectron spectroscopy (XPS) spectra were measured employing KRATOS (Amicus model) using the Mg target under 10^{-6} Pa pressure. The Raman spectra of the studied samples were obtained by DXRxi Raman imaging microscope by Thermo SCIENTIFIC with the excitation wavelength of 780 nm. The current-voltage (I-V) characteristics were obtained using Keithley 2450 source meter with the Science tech solar simulator class: AAA under solar illumination AM1.5 G.

3.3 Results and Discussion

3.3.1 X-ray Diffraction and microstructural studies

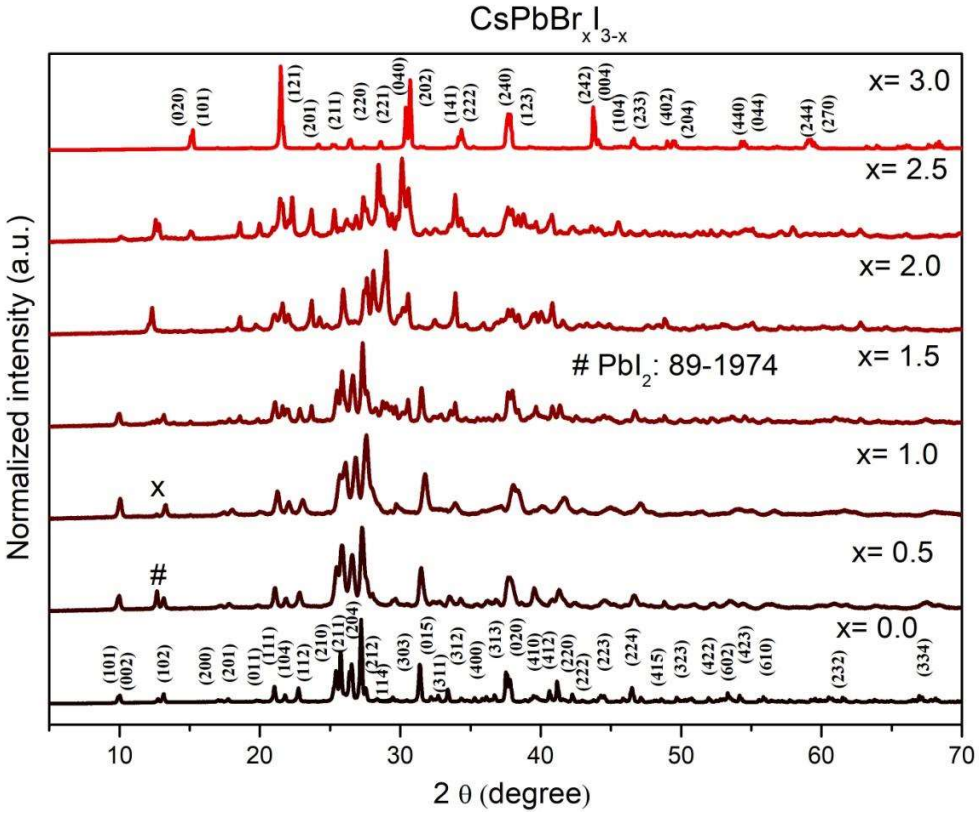

Figure 3.1: XRD patterns for $CsPbBr_xI_{3-x}$ (x= 0.0 - 3.0 in steps of 0.5) samples at room temperature.

Fig. 3.1 depicts the XRD patterns of $CsPbBr_xI_{3-x}$ (x= 0.0 - 3.0 in steps of 0.5). The XRD patterns up to x= 1.0 match with the indexing of $CsPbI_3$ (orthorhombic structure, *P*nma symmetry). A secondary phase observed at $2\theta \sim 12.62^o$ for x = 0.5 and 1.0, corresponds to PbI_2 (JCPDS file No. 89-1974). However, no peak corresponding to CsI and CsBr could be identified. A deep observation of $1.5 \leq x < 3.0$ suggests the mixing of peaks along with the parent compound $CsPbI_3$.

In order to identify a single or double phase, the Rietveld refinement of the samples has been done with the appreciable value of χ^2 ($1 < \chi^2 < 10$) using the FULLPROF software package. The values of Wyckoff positions are mentioned (Shown in table 3.1 and 3.2). We have done both the single and double phase refinement with P*nma* and P*nma*+ $R\bar{3}m$ symmetry corresponding to $CsPbI_3$ and PbI_2. Further, refinement of $CsPbI_3$ has been done using both the cif files corresponding to the perovskite (black) and non-perovskite phase (yellow). We have observed that the refinement is achieved with $CsPbI_3$ (yellow) and PbI_2 for x = 0.5 and x = 1.0 and pure $CsPbI_3$ is also refined using yellow orthorhombic phase (P*nma)* and double phase (P*nma* + $R\bar{3}m$) (Shown in Fig. 3.2). Fig. 3.3 shows the refinement of the XRD pattern with the single-phase parent compounds and double phase mixed halide compounds.

Table 3.1: Shows the fitting parameters with single phase for $CsPbBr_xI_{3-x}$ (x= 0.0, 0.5, 1.0,and 3.0) samples.

	Atom	**x**	**y**	**z**	**χ^2**
x = 0.0	Cs	0.41564	0.25	0.67009	17.8
	Pb	0.15985	0.25	0.43754	
	I1	0.16135	0.25	0.00103	
	I2	0.03326	0.25	0.61543	

	I3	0.30063	0.25	0.28508	
x = 0.5	Cs	0.42142	0.25	0.67451	4.45
	Pb	0.16562	0.25	0.43719	
	I1	0.15995	0.25	0.0074	
	I2	0.03803	0.25	0.61636	
	Br1	0.29699	0.25	0.27772	
x = 1.0	Cs	0.41807	0.25	0.66864	1.61
	Pb	0.16438	0.25	0.43575	
	I1	0.16567	0.25	-0.0003	
	I2	0.03877	0.25	0.61787	
	Br1	0.30248	0.25	0.28663	
x = 3.0	Pb	0	0.5	0	6.02
	Cs	-0.49384	0.25	0.00748	
	Br1	0.28938	0.47902	0.20666	
	Br2	0.03285	0.75	0.03956	
	Br3	-0.26975	0.65439	0.03477	

Table 3.2: Shows the fitting parameters with double phase for $CsPbBr_xI_{3-x}$ (x= 0.0, 0.5, and 1.0) and single phase of x=3.0 samples.

	Atom	**x**	**y**	**z**	χ^2
x = 0.0	Cs	0.41564	0.25	0.67009	17.8
$\mathbf{Pnma + R\bar{3}m}$	Pb	0.15985	0.25	0.43754	
	I1	0.16135	0.25	0.00103	
	I2	0.03326	0.25	0.61543	
	I3	0.30063	0.25	0.28508	
	Cs	0	0	0	
	Pb	0	0	0.44742	

	I1	0.152	-0.152	0.51048	
	I2	0.84284	0	0	
	I3	0.66362	0	0.50	
	I4	0.66362	0	0.50	
	I5	0	0	-0.4493	
x = 0.5	Cs	0.42142	0.25	0.67451	3.98
$Pnma + R\bar{3}m$	Pb	0.16562	0.25	0.43719	
	I1	0.15995	0.25	0.0074	
	I2	0.03803	0.25	0.61636	
	Br1	0.29699	0.25	0.27772	
	Cs	0	0	0	
	Pb	0	0	0.45054	
	Br1	0.4489	-0.44890	0.51135	
	Br2	0.35900	0	0	
	I1	0.68320	0	0.50	
	I2	0.68320	0	0.50	
	I3	0	0	-0.50472	
x = 1.0	Cs	0.41807	0.25	0.66864	1.61
$Pnma + R\bar{3}m$	Pb	0.16438	0.25	0.43575	
	I1	0.16567	0.25	-0.0003	
	I2	0.03877	0.25	0.61787	
	Br1	0.30248	0.25	0.28663	
	Cs	0	0	0	
	Pb	0	0	0.51135	
	Br1	0.44890	-0.44890	0.51135	
	Br2	0.35900	0	0	
	I1	0.68320	0	0.50	
	I2	0.16790	0.27100	0.33360	

	I3	0	0	-0.20620	
x = 3.0	Pb	0	0.5	0	6.02
Pnma	Cs	-0.49384	0.25	0.00748	
	Br1	0.28938	0.47902	0.20666	
	Br2	0.03285	0.75	0.03956	
	Br3	-0.26975	0.65439	0.03477	

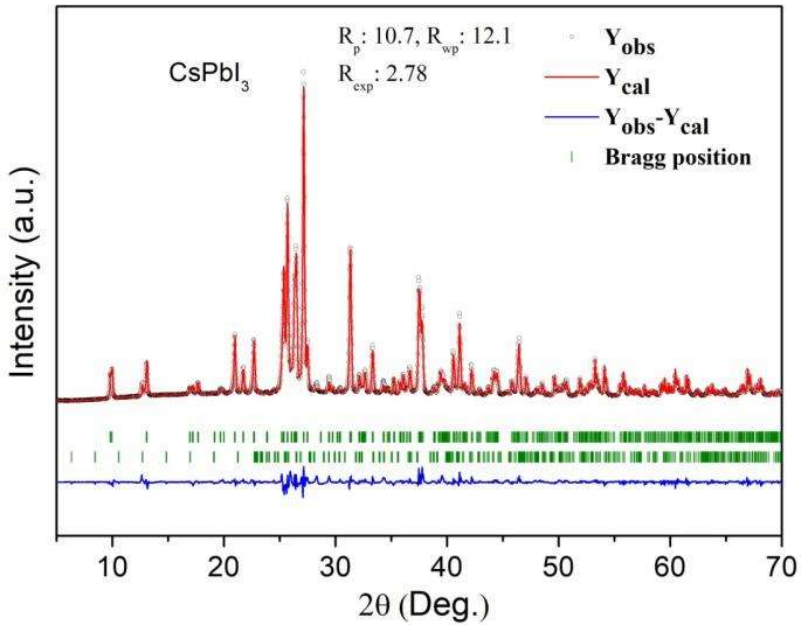

Figure 3.2: Double phase refinement of $CsPbI_3$.

The phase % corresponding to phase 1 and phase 2 are phase 1: 97.24% and phase 2: 2.76% for x = 0.5 and for x = 1.0; phase 1: 99.83% and phase 2: 0.17%. On the contrary, the XRD pattern corresponding to $1.5 \leq x < 3.0$, could not be well fitted with the single-phase due to the presence of extra XRD peaks of various phases as shown in Fig.3.4. The XRD patterns are analyzed using JCPDS file formats for the indexing of peaks and compared with the standard JCPDS file as shown in Fig. 3.4(a) for $1.5 \leq x < 3.0$. It is observed that for $1.5 \leq x <$

3.0, XRD patterns match with that of $CsPbBr_3$, $CsPbI_3$, PbI_2 and $PbBr_2$ and Pb_2O_3. Fig.3.4(b) shows the marking of each peak corresponding to the observed phases. Further, the percentage of phases obtained from XRD and ratio of intensity are shown in Table 3.3. Thus, our analysis suggests the formation of yellow phase of $CsPbI_3$ with some unreacted precursor PbI_2 for $0.0 \leq x = 1.0$. For $1.5 \leq x < 3.0$, mixture of phases corresponding to $CsPbBr_3$, $CsPbI_3$, PbI_2 and $PbBr_2$ are observed. This is possibly due to the decomposition of $CsPbI_3$ to PbI_2 and $CsPbBr_3$ to $PbBr_2$ upon oxygenation.

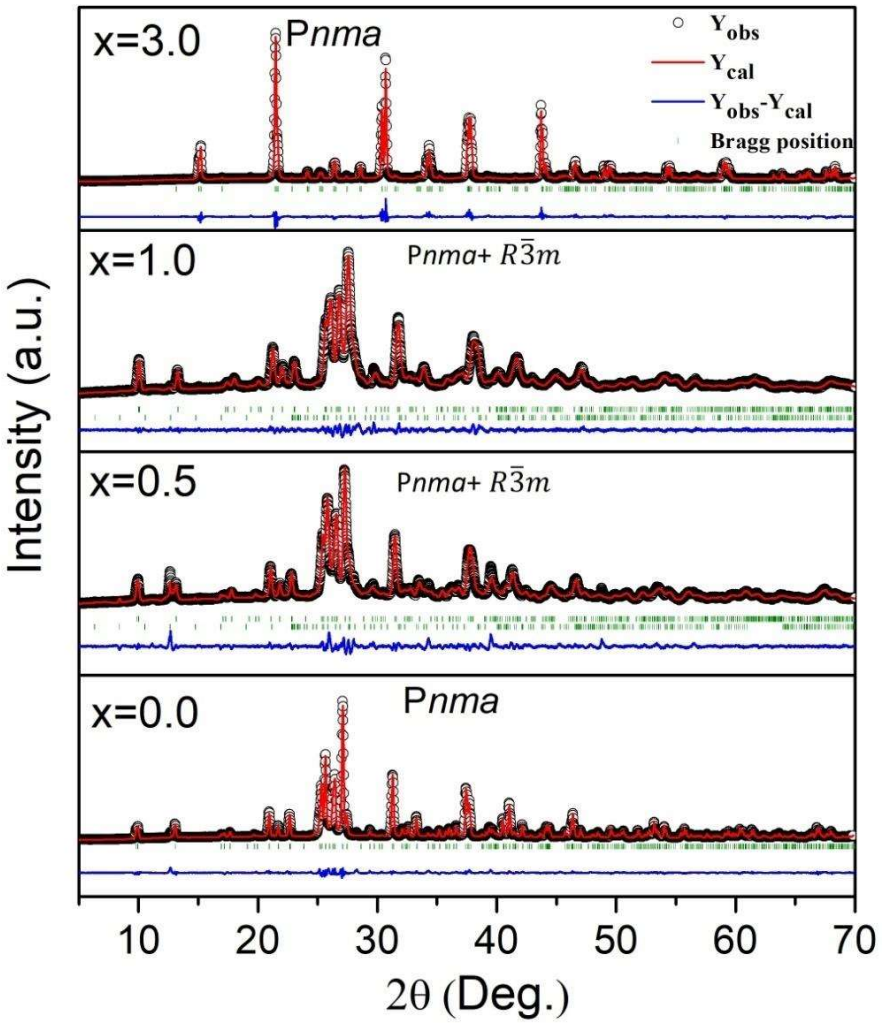

Figure 3.3: Rietveld refinement of XRD patterns of $CsPbBr_xI_{3-x}$ (x= 0.0, 0.5, 1.0, and 3.0) samples.

Table 3.3: The percentage of phases obtained from XRD and ratio of intensity.

Table:								
Composition	XRD				Band edge			
	Phase I Yellow non-perovskite phase $CsPbI_3$	Phase II PbI_2	Phase III Perovskite $CsPbBr_3$	Phase IV Perovskite $PbBr_2$	Phase I Yellow non-perovskite phase $CsPbI_3$	Phase II PbI_2	Phase III Perovskite $CsPbBr_3$	Phase IV Perovskite $PbBr_2$
X = 0.0	99.45 (0.00)*	0.55 (0.00)			2.74	2.33		
X = 0.5	97.24 (0.00)*	2.76 (0.00)			2.76	2.33		
X = 1.0	99.83 (0.00)*	0.17 (0.00)			2.78	2.35		
X = 1.5	91#	8.7	0.64	0.32	2.77	2.33		
X = 2.0	40#	19	32	9		2.3		2.84
X = 2.5	35#	13	40	21.5			2.24	2.86
X = 3.0			100				2.26	
*-obtained from Refinements								
#-obtained from raw XRD								

The lattice parameters obtained from Rietveld refinement of the $CsPbBr_xI_{3-x}$ (x= 0.0 - 3.0 in the steps of 0.5) up to x = 1.0 are shown in Fig. 3.5 (a and b), while lattice parameters for $1.5 \leq x < 3.0$ are obtained manually. It is observed that lattice parameters 'a' and 'c' are observed to decrease up to x = 1.0 and thereafter, no consistent variation is observed. This can also be seen through the shifting of diffraction peak (212) corresponding to $2\theta \approx 27°$ of the

$CsPbI_3$ (x=0.0) sample to a higher angle with the Br^- substitution leading to the lattice contraction as the ionic radius of Br^- ion is smaller than I^- ion.

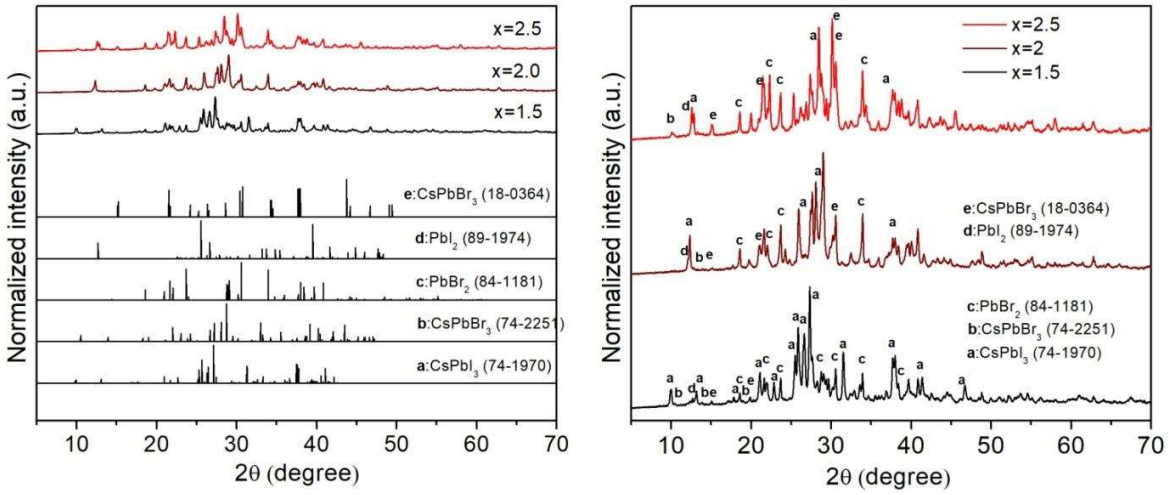

Figure 3.4: (a) Comparison of XRD patterns of $1.5 \leq x < 3.0$ with standard JCPDS files and (b) The indexing of every peak with various phases such as $PbBr_2$, PbI_2, $CsPbBr_3$ in the monoclinic and orthorhombic phases etc. for $1.5 \leq x < 3.0$.

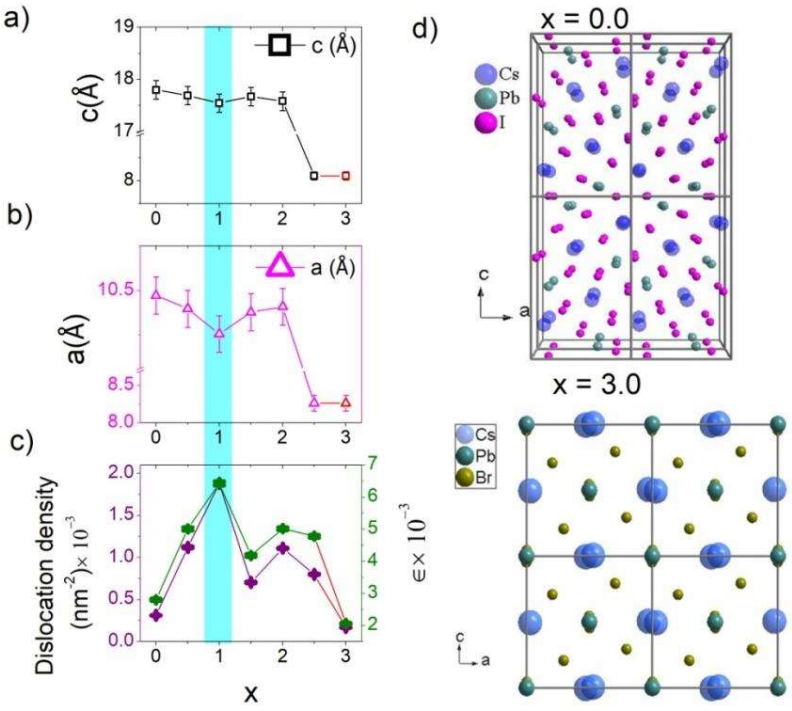

Figure 3.5: (a, b) Variation of lattice parameters 'a', 'c', with x (c) variation of dislocation density and microstrain with x and (d) Structure of $CsPbI_3$ and $CsPbBr_3$ plotted with Diamond using cif file obtained from Rietveld refinement.

The dislocation density ($\boldsymbol{\delta}$) and microstrain ($\in$) of the materials were calculated from the experimental XRD data (Fig. 3.4(c)) using the formula $L = \frac{K\lambda}{\beta \cos\theta}$, $\delta = \frac{1}{L^2}$, $\in = \frac{\beta}{4 \tan\theta}$, respectively [142] and showing the maximum values at x = 1.0, where, K, λ, θ, and β are the Scherrer constant, the wavelength of X-ray, the diffraction angle, and the full width at half maximum (FWHM), respectively. Further, for the illustration of the non-perovskite phase, structures of x = 0.0 and 3.0 are shown in Fig. 3.5(d).

The lattice parameters suddenly increased with the reduction in microstrain, and dislocation density as illustrated in Fig. 3.5. The change in behavior of lattice parameters, microstrain, and dislocation density for $x \geq 1.5$ is further analyzed through SEM and DSC. To further understand the distribution of grains observed with the bromide content, SEM micrographs are recorded (Fig. 3.6). The grain size distribution histograms (insets of fig. 3.6) are analyzed using Image J software. The dense and well-connected grain morphology of faceted grains is observed for x = 0.0. However, with the Br content, the grain morphology gets porous. It can also be seen that the grain size is nearly constant up to x = 1.0 (i.e. 0.51 μm, 0.50 μm, 0.52μm) and further decreases at $x \geq 1.5$ (0.28 μm) up to x = 2.0. Further, grain size increases for $x > 2.0$. It can be correlated with the I content (from the experimental EDX data, Fig. 3.7) as a small atomic percentage of I indicates the small grain size at x=1.5. The change in grain/ grain boundary morphology can be explained by grain boundary roughening. The faceted grains are responsible due to the higher driving force at x = 0.0. When the grain-boundaries are rough (joined), a smaller driving force has changed the grain shape from faceted to porous with Br substitution in spite of the increase in grain size. The change in morphology with Br content is explained as follows. The transitions at grain boundaries from rough to

faceted depend upon the step-free energy or edge energy at the surface and grain boundary changes from faceted to rough with the reduction in step-free energy.

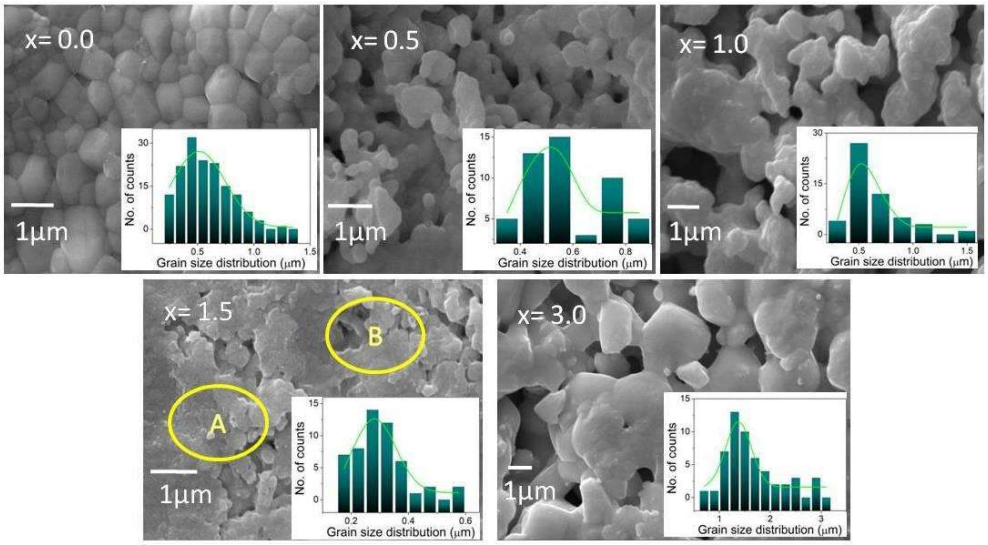

Figure 3.6: SEM micrographs of $CsPbBr_xI_{3-x}$ (x= 0.0, 0.5, 1.0, 1.5 and 3.0) samples. Circle A and B show grain boundary rupturing (degradation).

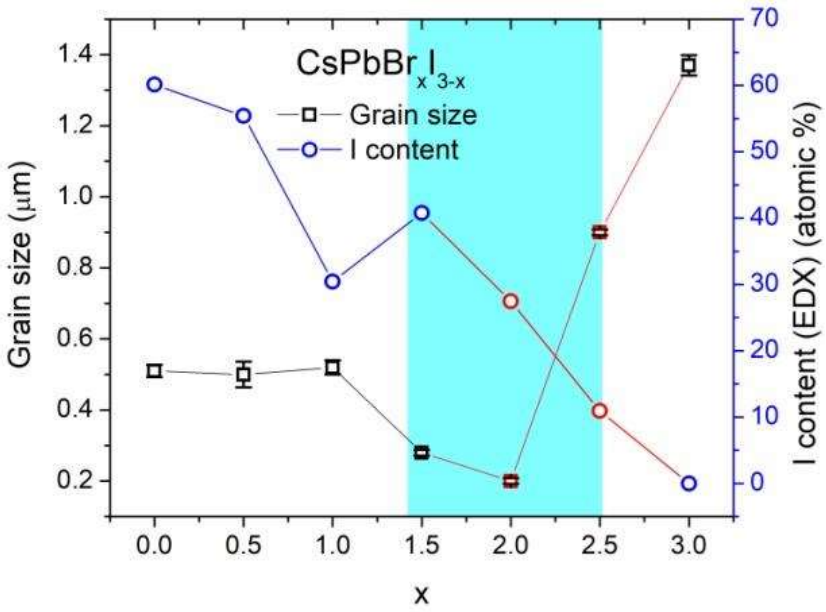

Figure 3.7: Variation of I content obtained from EDX and grain size analyzed from grain size histograms of $CsPbBr_xI_{3-x}$ (x= 0.0 - 3.0 in steps of 0.5) systems.

This surface roughening comes as a result of enhancement in entropy induced by the vacancy concentration. Further, an increase in the fraction of rough grain boundaries with the segregation of I vacancies at boundaries leads to the increase in step-free energy and the decrement in critical driving force, resulting in lower growth kinetics [143],[144],[145]. Hence, lower grain size at x = 1.5.

3.3.2 Thermodynamics

Figure 3.8(a) shows the variation of heat loss (ΔQ/Δm) with the temperature for Perovskite powders $CsPbBr_xI_{3-x}$ (x= 0.0, 0.5, 1.0, 1.5, and 3.0). One large exothermic peak is observed for each of the $CsPbBr_xI_{3-x}$ (x= 0.0, 0.5, 1.0, 1.5, and 3.0)samples at ~ 251 K, 253 K, 254 K, 255 K, and 250 K, respectively. Some small exothermic peaks can also be seen at ~ 272 K due to the major variation of the large exothermic peak at ~ 251 K.Figure 3.8(b) shows the variation of Gibbs free energy (ΔG) with temperature for $CsPbBr_xI_{3-x}$ (x= 0.0, 0.5, 1.0, 1.5, and 3.0) compounds. The value of Gibbs free energy (ΔG) for these samples are -40 J/mol, -50J/mol, -58J/mol, -68J/mol, and, -27J/mol at ~ 252 K, respectively. It is also observed that the values of entropy (ΔS) are 0.159 J/mol K, 0.123J/mol K, 0.070J/mol K, 0.097J/mol K, and 0.122J/mol K at ~ 252 K, respectively (Shown in Fig. 3.9). The value of Gibbs free energy suggests the lower formation temperature for x = 1.5 sample while others can be synthesized at a comparatively higher temperature. The endothermic peaks in heat capacity peaks are observed to shift with the composition suggest the different crystallization temperatures for the different x. Further, the entropy change is also reflecting the change in morphology with Br content.

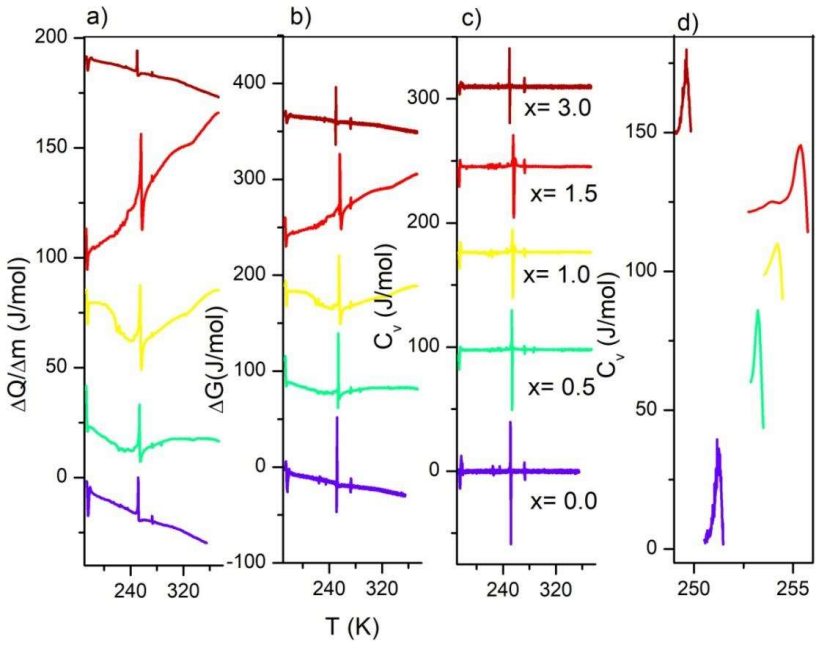

Figure 3.8: (a) Variation of (ΔQ/Δm) with temperature(b) Variation of (ΔG) with temperature (c) Variation of (C_v) with temperature (d) Schottky Anomaly variation for $CsPbBr_xI_{3-x}$ (x= 0.0, 0.5, 1.0, and 3.0) systems.

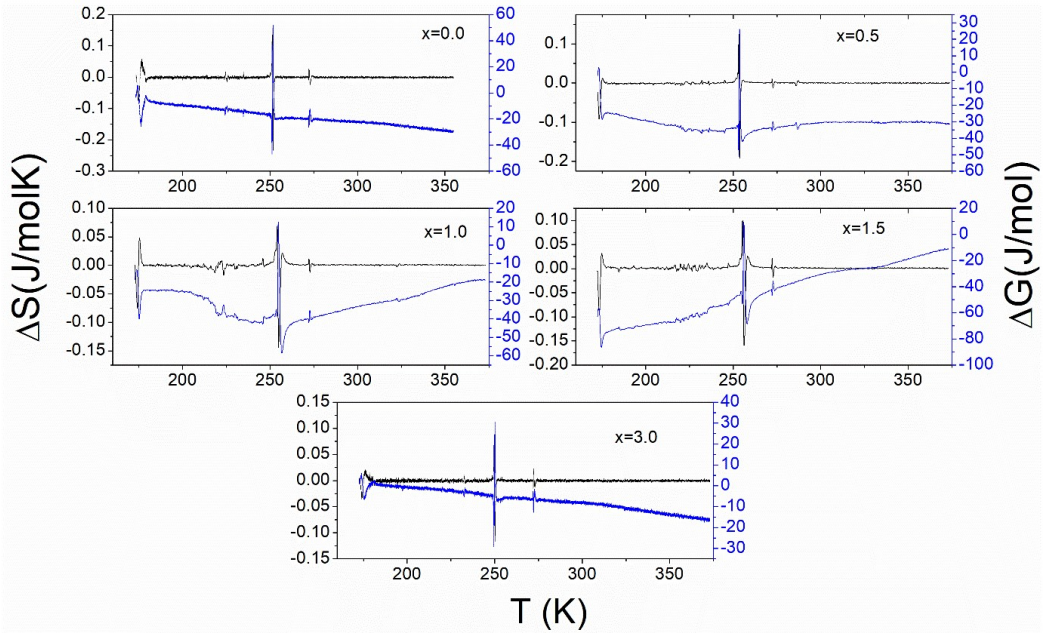

Figure 3.9: The change in Gibbs free energy (ΔG) and entropy (ΔS) with temperature and showing Little change in the entropy of these compounds indicates that the samples are thermodynamically stable at room temperature.

In the specific heat curves (Fig. 3.8(c)), there is a spike at ~251 K, 253 K, 254 K, 255 K, and 250 K, respectively. It is also observed that the specific heat (C_V) for $CsPbBr_xI_{3-x}$ (x= 0.0, 0.5, 1.0, 1.5, and 3.0) samples at these temperatures are 37 (J/mol), 31 (J/mol), 18 (J/mol), 25 (J/mol), and 29 (J/mol), respectively. The specific heat of the samples is observed to decrease with the Br content, while it increases for $x \geq 1.5$. The value of specific heat indicates the thermal sensitivity of the samples. Thus, small specific heat shows the more thermal sensitivity of the materials [146]. It can also be concluded that the thermal sensitivity increases with the increase in the Br content up x = 1.0 and thereafter it decreases. Further, specific heat curves (Schottky anomaly at ~ 250K) (Fig. 3.8(d)) are fitted according to the relation "$C_V = C_{el} + C_{ph} = \gamma T + \beta T^3$ where $\gamma = (2/3)\pi k_B^2 N(E_F)$ and $\beta = 12\pi^4 N_A k_B / 5\Theta_D^3$, N = N_A, Avogadro number, $N(E_F)$ is the density of states at Fermi level, and Θ_D is Debye temperature". It is observed that C_v data corresponds to the density of states (DOS) of a double-phase as Schottky anomaly comprises two peaks for $0.0 \leq x \leq 1.0$. Further, C_v curve of x = 1.5 exhibits more peaks rather than one corresponding to the different DOS due to the two or more phases [147]. Moreover, the peak is observed to shift towards higher temperature indicating different formation temperatures with compositions. This can be attributed to the variation of strain with Br content.

3.3.3 Optical Properties

Fig. 3.10(a) shows the absorbance spectra for $CsPbBr_xI_{3-x}$ (x= 0.0 to 3.0 at the step of 0.5) samples. Two major absorbance edges (I and II) are observed for composition $x < 3.0$. For x= 3, i.e., $CsPbBr_3$ the maximum and broad absorbance edge is appearing at ~ 550 nm. To identify the absorbance edges clearly, a differential absorbance plot ($d_E\sqrt{A}$) is plotted which shows the peaks at the band edges. For $x \geq 2.5$, a peak is observed at ~ 533 nm (E = 2.33 eV). Apart from

this, two major peaks are appearing at ~ 2.35 eV and ~2.85 eV. Further, the Tauc plot is plotted to estimate the direct bandgap energy for these samples and bandgap energy corresponds to the peak observed in Fig. 3.10(b). The estimated bandgap energy corresponding to edges is plotted in Fig. 3.10(d). Interestingly, the bandgap corresponding to edge II (grey strip) belongs to PbI_2 [148], and edge I (orange strip) corresponds to the yellow non-perovskite phase of $CsPbI_3$.

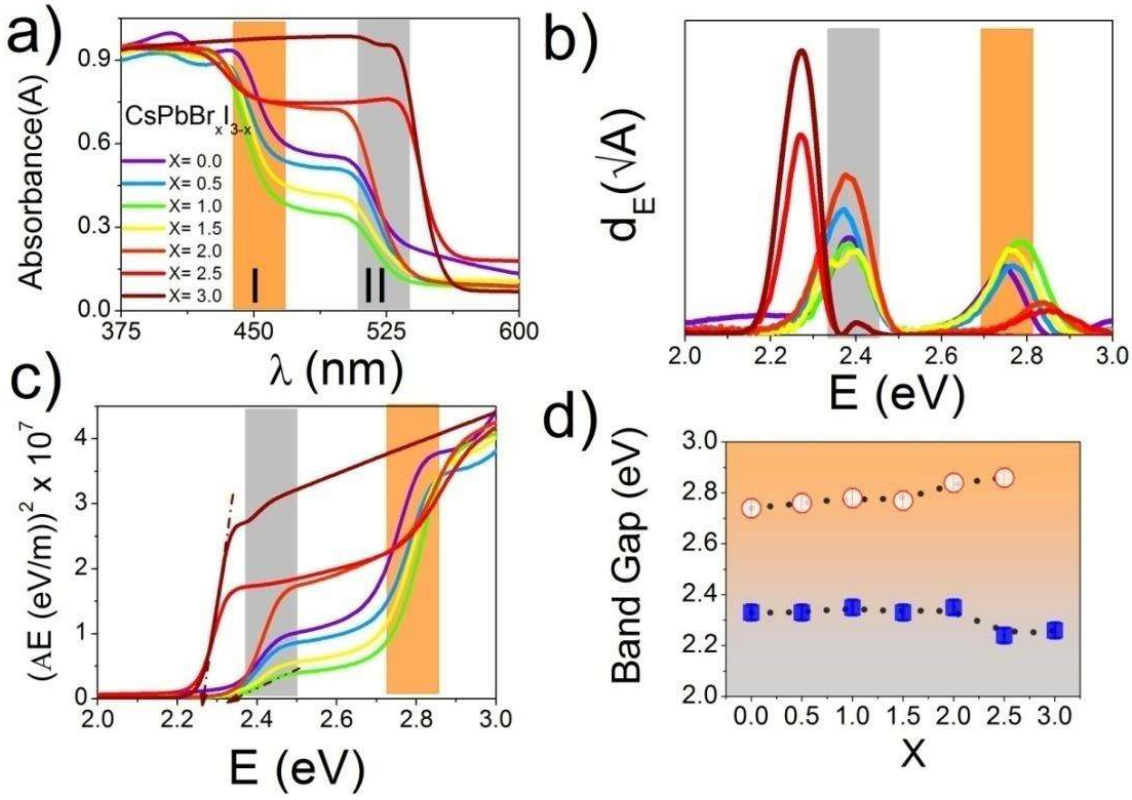

Figure 3.10: (a) Absorbance spectra for $CsPbBr_xI_{3-x}$ (x= 0.0 to 3.0 at the step of 0.5) samples (b) Differential absorbance showing peaks at the band edges (c) Tauc plot for $CsPbBr_xI_{3-x}$ (x= 0.0 to 3.0 at the step of 0.5) samples (d) Energy band gap at two indicated band edges (I and II) for $CsPbBr_xI_{3-x}$ (x= 0.0, 0.5, 1.0, 1.5, and 3.0) samples.

3.3.4 XPS Studies

As mentioned earlier, there is a degradation for x ≥ 1.5 samples while synthesis in the ambient atmosphere via cold sintering technique. Thus, elemental states and the presence of O have been studied using XPS studies.

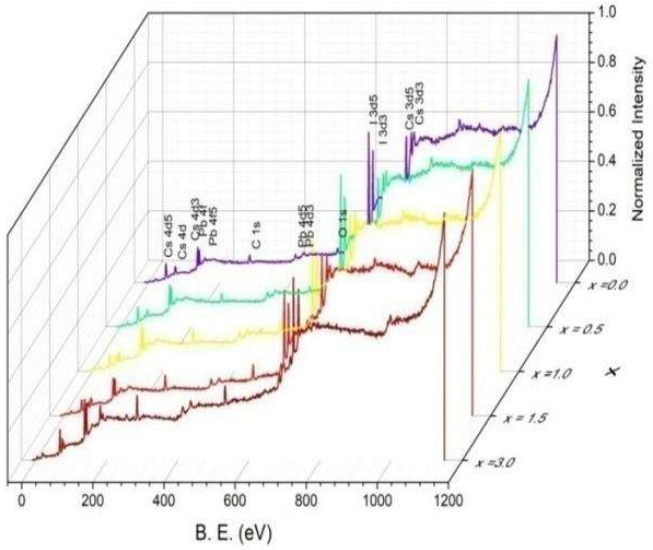

Figure 3.11: Wide range XPS spectrum of $CsPbBr_xI_{3-x}$ (x= 0.0, 0.5, 1.0, 1.5 and 3.0) systems.

XPS wide spectra (Fig. 3.11) and elemental spectra are calibrated with carbon (C) 1s peak at 284.5 eV from the (NIST) XPS database [149]. After analyzing the XPS data, the Cesium spectrum reveals two peaks $3d_{3/2}$ and $3d_{5/2}$ for x=0.0, corresponding to the binding energies of 738.69 eV and 724.58 eV, respectively (Fig. 3.12) and lead (Pb) element shows Pb $4f_{7/2}$ and Pb $4f_{5/2}$ peaks for x = 0.0 corresponding to the binding energies 137.63 eV and 142.59 eV, respectively (Fig. 3.12). The peaks of I (x = 0.0) and Br (x = 0.5) related to I $3d_{3/2}$,I $3d_{5/2}$, Br $3d_{3/2}$, Br $3d_{5/2}$ are located at 630.53 eV, 619.15 eV, 68.75 eV, and 67.22 eV, respectively, shown in Fig. 3.13. The values of the binding energy of the constituent elements are in

accordance with the reported literature [150]. In Br and I spectra, satellite features are observed (arrow sign) at ~ 65 eV and ~ 623 eV, respectively [151].

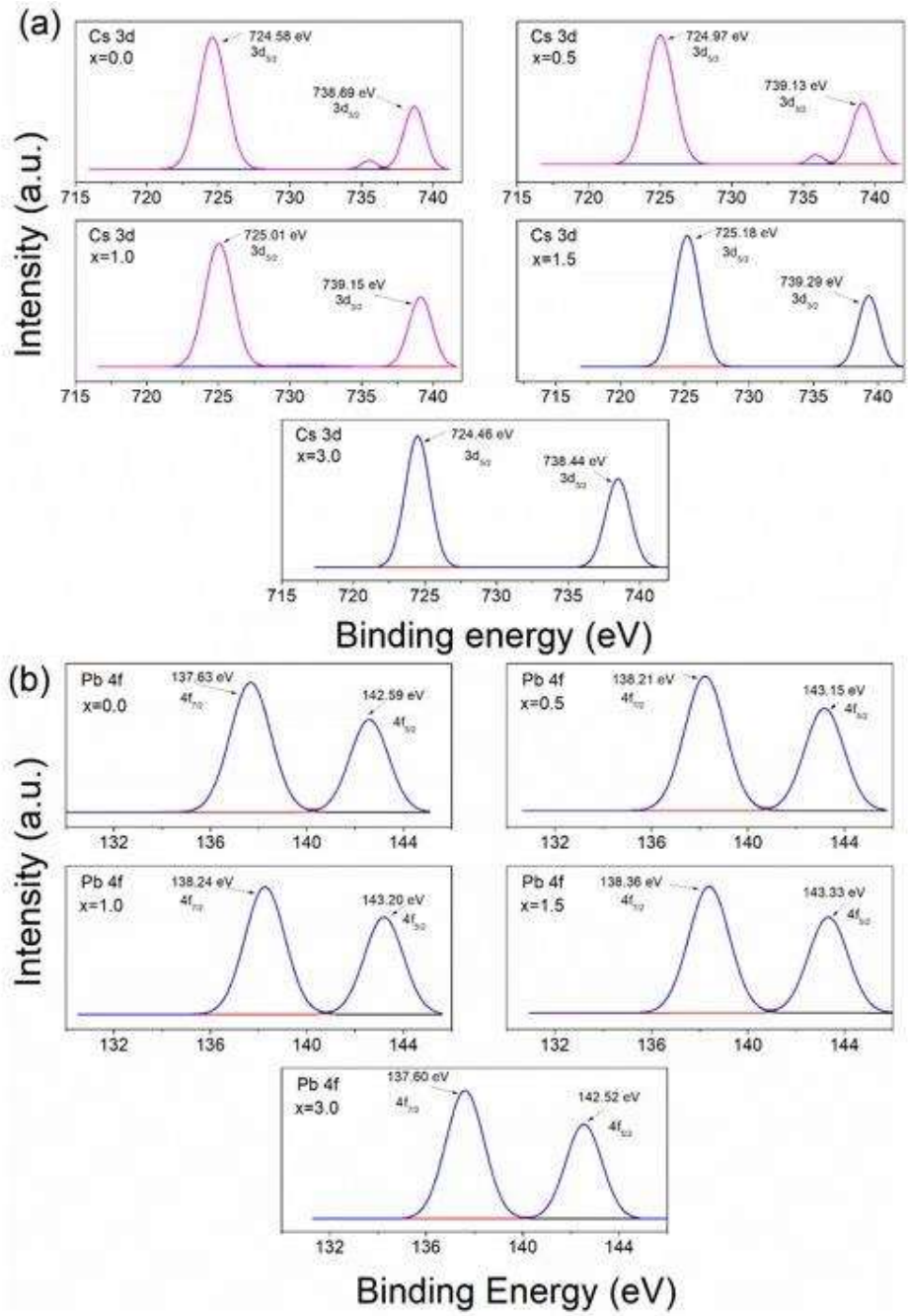

Figure. 3.12: XPS spectra with peak fitting of $CsPbBr_xI_{3-x}$ (x=0.0, 0.5, 1.0, 1.5, and 3.0) corresponding to (a) Cs 3d; and(b) Pb 4f.

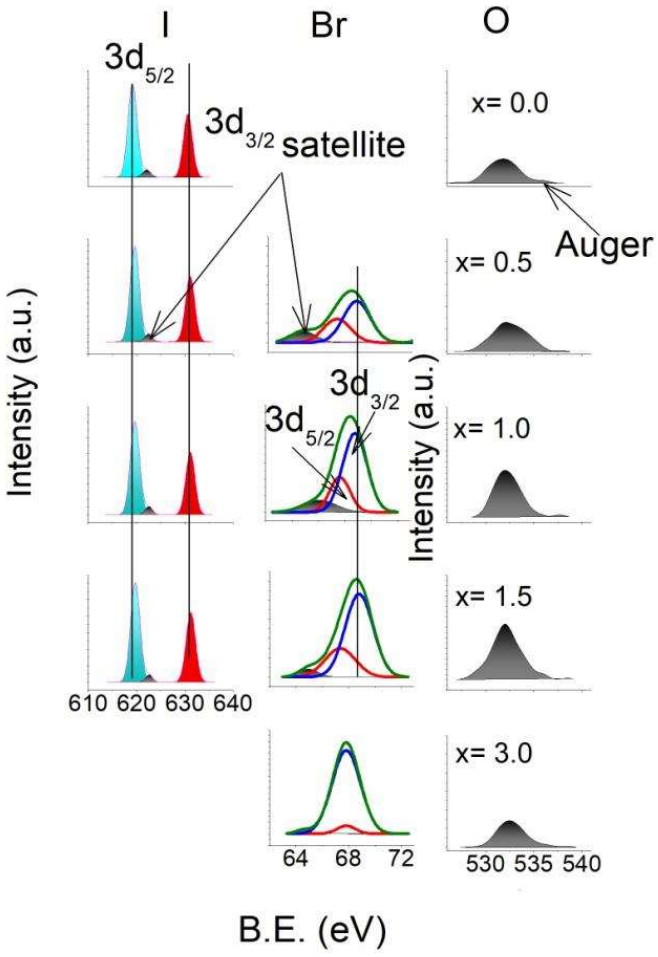

Figure 3.13: XPS spectra with peak fitting of $CsPbBr_xI_{3-x}$ (x=0.0, 0.5, 1.0, 1.5, and 3.0) corresponding to (a) I 3d (b) Br 3d and (c) O (2p).

It is observed that the peak position corresponding to $3d_{5/2}$ in I spectra is observed to shift with x suggesting the change in oxidation states of I [152]. Moreover, the intensity of peak corresponding to $3d_{3/2}$ in I spectra is lowest at x = 1.0 suggesting maximum I vacancy formation. Further, no shifting is observed in Pb, Cs, Br, and O confirming that all the elements are in their respective valence states [153]. In O spectra, intensity is higher at x = 1.5 with the formation of Auger peaks. Thus, electron transfer between I, Br, and O is leading to the

degradation at $1.5 \leq x < 3.0$. This degradation is further observed using impedance spectroscopy.

3.3.5 Electrical Studies

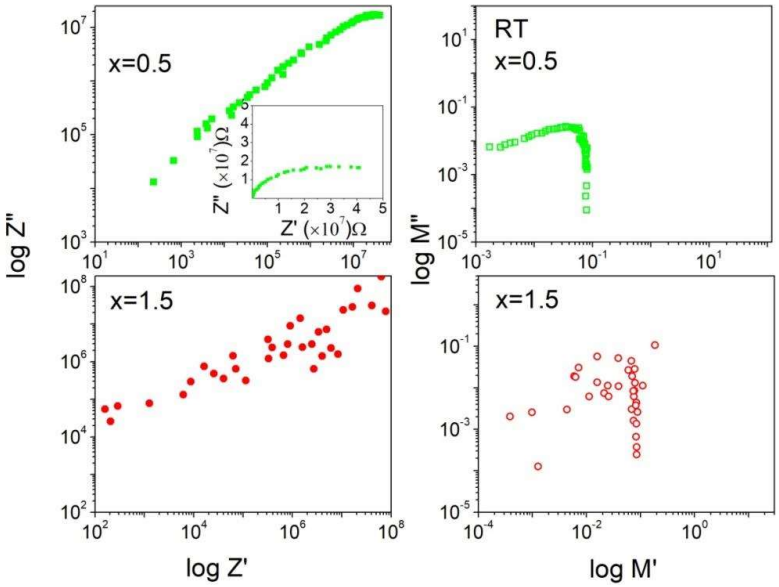

Figure 3.14: Impedance and Modulus Nyquist plots for $CsPbBr_xI_{3-x}$ (x=0.5 and 1.5) showing grain disintegration.

It can be seen from impedance Nyquist plots that grain has disintegrated at x= 1.5 instead of x = 0.5 (Fig. 3.14) owing to the presence of a depressed semicircular arc (Fig. 3.14 inset). To verify grain disintegration, complex electric modulus has been plotted as it resolves the grain and grain-boundary effects after suppressing the electrode effects. At x = 0.5, a single arc is observed confirming the single-phase nature of the composition while the same could not be observed at x = 1.5 (shown in Fig. 3.14). Moreover, the asymmetric semicircular arc indicates the relaxation mechanism of charge carriers. Thus, grain disintegration with the absence of a relaxation mechanism can be concluded at x = 1.5.

3.3.6 Current (*I*)-Voltage (*V*) Studies

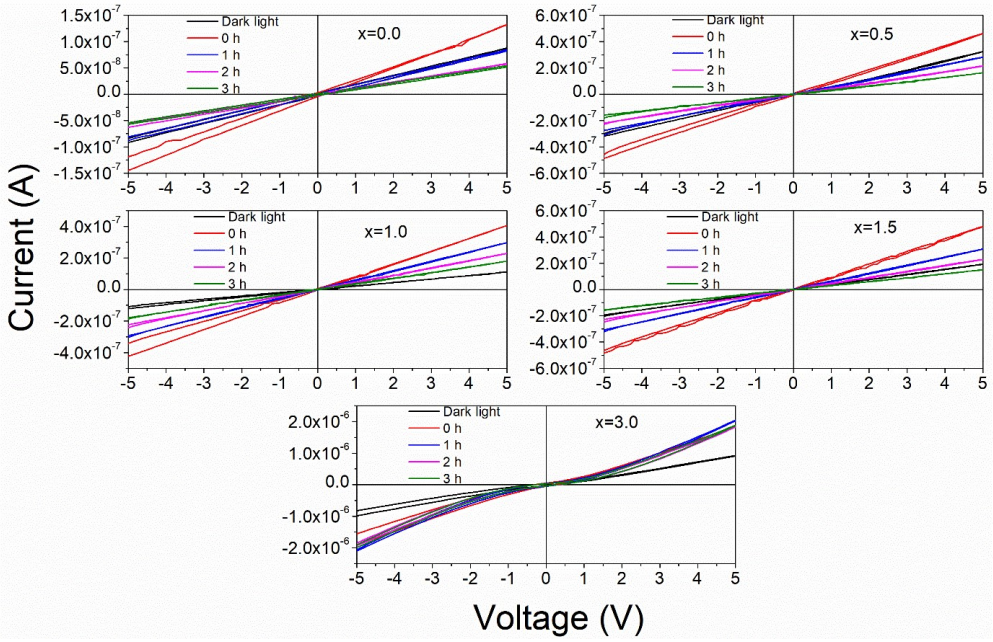

Figure 3.15: Current (I) - voltage (V) curves for $CsPbBr_xI_{3-x}$ (x = 0.0, 0.5, 1.0, 1.5, and 3.0) samples.

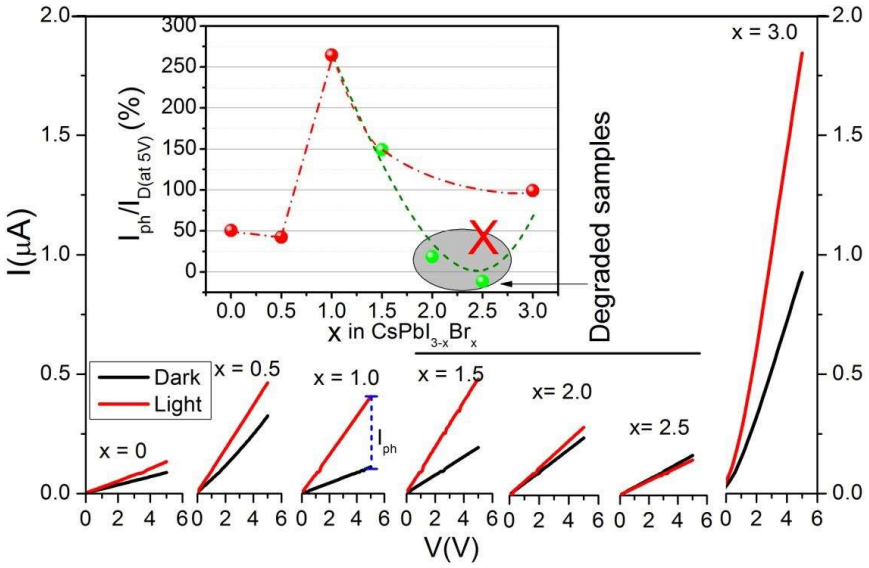

Figure 3.16: Current (I) - voltage (V) curves for $CsPbBr_xI_{3-x}$ (x= 0.0 - 3.0 in steps of 0.5) samples. Inset shows compositional variation of ratio of photocurrent to the dark current at 5V.

Further, to check the photostability of these compounds in sunlight exposure, the current-voltage (I-V) curves were recorded. The output current of these samples was recorded for 3 hours (every 60 minutes) in the continuous exposure of AM 1.5G sunlight and observed that the samples are stable (see Fig. 3.15). Fig. 3.16 shows the I-V plot of the samples in the dark and exposure of AM 1.5G sunlight. It is observed that $CsPbBr_3$ (x = 3.0) and $CsPbI_3$ (x = 0) has the highest and lowest value of current at given voltage respectively, for the studied compositions here. The high value of dark current and photocurrent for x = 3.0 can be attributed to the highest and broad absorbance. However, with the substitution of Br, the trend is not uniform as it is also suggested by the deviation from Vegard's law (Fig. 3.17) after x = 1.0. The photo field generated current (I_{ph}) has been estimated at +5V biasing as the difference between dark current (I_D) and current after exposure. The percent relative variation of I_{ph} with respect to the dark current is estimated and plotted as an inset of Fig. 3.16. This suggests maximum I_{ph} for the x = 1.0 thereafter photogeneration is decreased significantly. This compositional behavior is in accordance with the above structural, optical, and dielectric studies as x = 1.0 show the least traces of PbI_2 while $1.5 \leq x < 3.0$ has multiple phases as suggested from the deviation pattern from Vegards line (Fig 3.17) showing volumetric expansion.

In order to predict the degradation mechanism and non- perovskite phase formation, activation energy (Fig. 3.18(a)) has been estimated from the Arrhenius plots of Gibbs' free energy (Fig. 3.18(b)). The variation of ln(ΔG) vs 1000/T for x = 0.0 and 3.0 is shown in Fig. 3.18(b). It is observed that I containing samples showed the activation energy, $E_a \leq 0.08$eV suggesting the formation of $V_I^{\bullet}$ [82]. Further, for x = 3.0, it seems that there is formation of

Br_{Cs}^{2-} [109] below RT (T < 351K) but we observed Br^- ion migration in the grain boundary region (E_a= 0.48eV, T > 351K) [140].

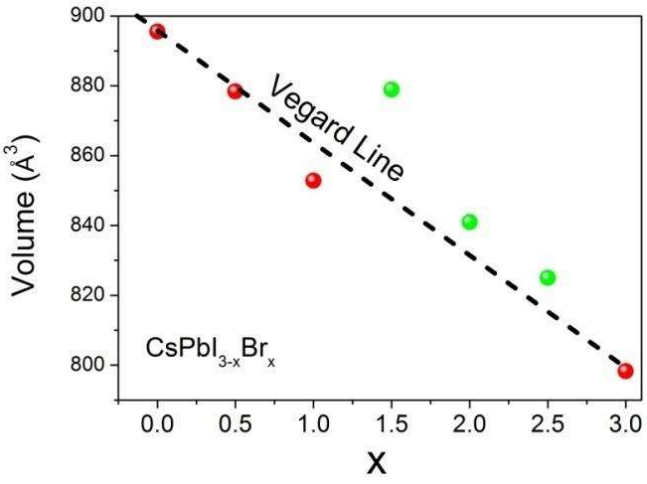

Figure 3.17: Deviation of Vegard's law for $CsPbBr_xI_{3-x}$ (x= 0.0 - 3.0 in steps of 0.5) samples.

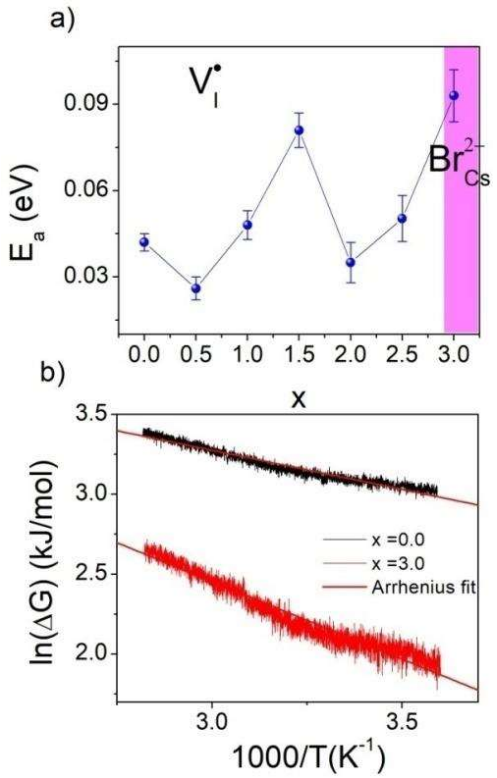

Figure 3.18: (a) Activation energy of $CsPbBr_xI_{3-x}$ (x= 0.0 to 3.0 at the steps of 0.5). (b) Variation of ln(ΔG) vs 1000/T for x = 0.0 and 3.0

In order to confirm the oxygenation, Raman spectroscopy has been used (Fig. 3.19(a)). We have observed modes corresponding to polymorphs of Pb-O ($Pb_mO_{m+\delta}$) and Pb-I bond. Among the degraded compositions, for x = 2.0 and 2.5, prominent peak corresponding to $Pb_mO_{m+\delta}$ is observed. While, for x = 1.5, the sharp peak corresponds to PbI_2 is clearly observed. However, some small relative intensity of $Pb_mO_{m+\delta}$ is also observed for x = 1.5. Further, we have plotted area of peaks corresponding to metal-O and metal-OH bond in XPS spectra corresponding to O (Fig. 3.19(b)). We have observed that area corresponding to metal-OH peak is steadily increasing with x but for $1 \leq x \leq 2$, area corresponding to metal-O peak is nearly constant i.e. transforming from Pb-I influenced region to Pb-O influenced region. On interaction of $CsPbI_3$ with moisture, PbI_2 reacts with H_2O to form PbO and HI but this depends on moisture and PbO and HI further reacts to form PbI_2 and H_2O. This interaction is depending on I/Br ratio which is also leading to some other byproducts and leading this reaction to a typical irreversible reaction.

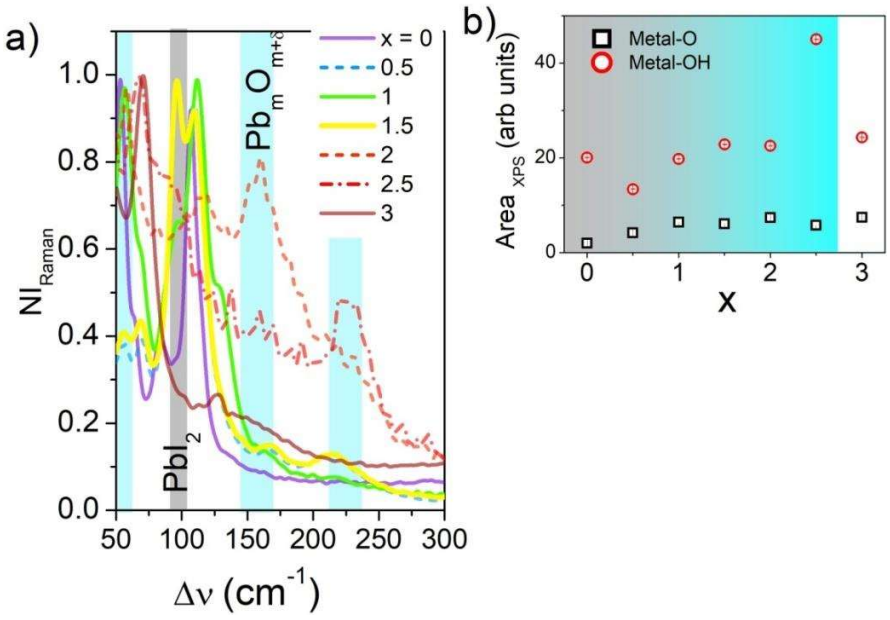

Figure 3.19: (a) Raman spectra of $CsPbBr_xI_{3-x}$ (x= 0.0 to 3.0 at the steps of 0.5). (b) Area of peaks corresponding to metal-O and metal-OH bond in O XPS spectra.

As these perovskites are more prone to moisture, light and oxygen and oxygenation of the samples in cold-sintering technique is not only process-dependent but also composition dependent. From the above studies, intensity of $Pb_mO_{m+\delta}$ observed in Raman and constant area corresponding to metal-O peak in XPS and lack of signal in XRD and grain boundary degradation suggests the transformation from Pb-I influenced region to Pb-O influenced region. The mechanism of degradation is illustrated as follows:

$$CsPbX_3 + \frac{1}{2}O_2 \xrightarrow{\Delta_{80}\,^oC} PbO + CsX + X_2$$

Thus for the smaller grain size samples - the mixing of halides (I/Br) encourages degradation by reducing the grain size (and thereby increasing the surface area).

3.4 Conclusion

The $CsPbBr_xI_{3-x}$ (x= 0.0, 0.5, 1.0) compounds prepared by the cold sintering are observed to be double phase with P*nma*+ $R\bar{3}m$ symmetry in yellow non-perovskite phase. The compound with $1.5 \leq x < 3.0$ indicate various phases with and without oxygen including the $CsPbBr_3$ (orthorhombic, *P*nma) phase. With the incorporation of Br, I sites are occupied by Br^- ions leading to the creation of positive $V_I^{\bullet}$, I incorporation at A – site (Cs) leaving space for the formation of PbI_2 and PbO as confirmed from Raman analysis. From XPS analysis for oxygen, area corresponding to metal-OH peak is steadily increasing with x but for $1 \leq x \leq 2$, area corresponding to metal-O peak is nearly constant i.e. transforming from Pb-I influenced region to Pb-O influenced region. This interaction is depending on I/Br ratio which is also leading to some other by products and leading this reaction to a typical irreversible reaction.